Electrostatic Fields Due to an Electrode Mounted on a Conducting Pad of Finite Extent in a Planar Stratified Medium

JEAN-FU KIANG, TAREK M. HABASHY, MEMBER, IEEE, AND JIN AU KONG, FELLOW, IEEE

Abstract—**The quasistatic fields generated by an electrode mounted on a perfectly conducting pad of finite extent and embedded in a planar stratified medium are analyzed. An integral equation in the spectral domain is derived for the outflowing current density distribution on the pad-electrode surface. The method of moments is then applied to solve the integral equation. The effects of the electric properties of the stratified medium and the standoff thickness on the total electrode current are investigated. Several conductivity profiles modeling different practical measurement environments are also considered.**

I. Introduction

THE ROUTINE APPLICATION of resistivity sounding measurement in geophysical exploration started with the work of Wenner in 1915 and Schlumberger in 1920 [1]–[5], both using a four-terminal electrode array. The dipole array [1] has also been routinely used, which is a modified version of the Wenner array.

In geophysical prospection for oil, a borehole is drilled in the earth. The borehole is filled with mud to balance the down-hole pressure. The conductivity of the mud is usually higher than the conductivity of the surrounding rock formation. The mud may flush into the rock formation, generating an invaded zone behind the borehole wall. Usually the conductivity of the invaded zone forms a profile with conductivity values varying between that of the mud and the rock formation.

In this paper we will consider a canonical problem that can be employed to study the physics of electrode tools that are routinely used in prospecting the conductivity of rock formations. Fig. 1(a) shows the geometry of the problem. A perfectly conducting electrode is mounted on a metallic pad of a finite extent. The pad is assumed to be perfectly conducting and has the effect of focusing the current into the formation. The pad-electrode arrangement is pressed against the borehole wall, injecting low-frequency currents into the rock formation.

To simplify the analysis, the geophysical environment is modeled as a planar stratified lossy medium [8], [9] as shown in Fig. 1(b). The pad is modeled as a perfectly conducting rectangular plate as shown in Fig. 2, and the electrode is modeled as a small rectangular patch located in the center of a hole on the pad surface and is isolated from the pad by an insulator. The pad is embedded in a planar stratified medium of an arbitrary number of layers.

In Section II, an electrostatic formulation in the spectral domain is introduced starting from a transverse magnetic (TM) wave formulation. An integral equation in the current is then obtained by imposing the appropriate boundary condition on the pad-electrode surface. Expressions for the potential distribution in each layer are also derived.

In Section III, the method of moments is applied to solve the integral equation numerically. In Section IV, the numerical results are presented and discussed to investigate the performance of the pad-electrode as a geophysical tool. Different models representing the measurement environment are investigated. Four different types of conductivity profiles for the invaded zone are also considered.

Manuscript received July 8, 1988; revised November 10, 1988. This work was supported by Schlumberger-Doll Research, the Joint Services Program under Contract DAAL03-86-K-0002, ONR Contract N00014-86-K-0533, and NSF Grant 8620029-ECS.

J. F. Kiang and J. A. Kong are with the Department of Electrical Engineering and Computer Science, Massachusetts Institute of Technology, Cambridge, MA 02139.

T. M. Habashy is with Schlumberger-Doll Research, Ridgefield, CT 06877.

IEEE Log Number 8927852.

II. Problem Formulation

The geometrical configuration of an electrode mounted on a perfectly conducting pad buried in the lth layer of a stratified medium is shown in Fig. 1(b). The thickness and conductivity of the jth layer are h_j and σ_j, respectively. The pad is located at $z = z_p$.

The top view of the pad-electrode configuration is shown in Fig. 2. The pad is modeled as a rectangular plate with a square hole at the center. The electrode is modeled as a square patch located in the middle of the hole, and is electrically insulated from the pad.

We choose the coordinate system such that the centers of the pad and the electrode are at the origin, and the pad sides are parallel to the x and y axes. The widths of the pad along the x and y direction are denoted by w_p^x and w_p^y, respectively. Similarly, the widths of the hole are denoted by w_h^x and w_h^y, and those of the electrode by w_e^x and w_e^y.

Since in the low frequency limit, the problem reduces to an electrostatic one, we therefore consider only the TM_z field components. The z component of the electric field in the lth layer can be expressed as [9], [10]

$$\begin{aligned} E_{lz}(\bar{r}) = \iint_{-\infty}^{\infty} & d\bar{k}_s e^{i\bar{k}_s \cdot \bar{r}_s} \tilde{e}_l(\bar{k}_s) \\ & \cdot \left\{ \pm e^{ik_{lz}|z-z_p|} + \frac{1}{1 - R_{\cup l} R_{\cap l} e^{2ik_{lz}h_l}} \right. \\ & \cdot \left[R_{\cup l} e^{ik_{lz}(-z-z_p-2d_{l-1})} - R_{\cup l} R_{\cap l} e^{ik_{lz}(-z+z_p+2h_l)} \right. \\ & \left. \left. - R_{\cap l} e^{ik_{lz}(z+z_p+2d_l)} + R_{\cup l} R_{\cap l} e^{ik_{lz}(z-z_p+2h_l)} \right] \right\} \end{aligned} \quad (1)$$

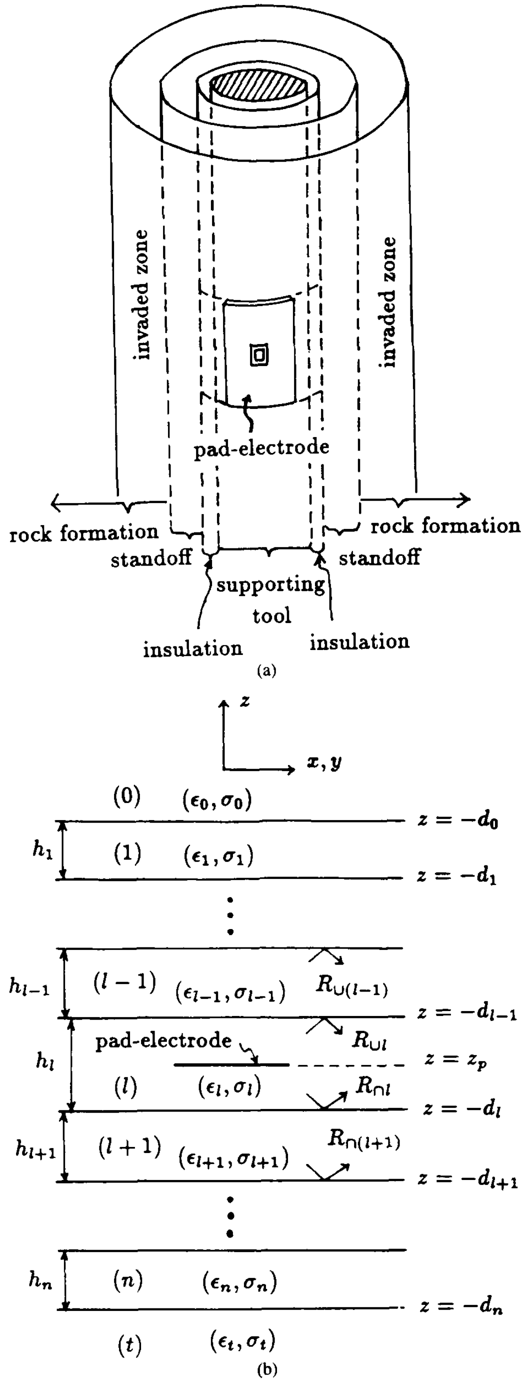

Fig. 1. (a) Geometrical configuration of a pad-electrode embedded in the borehold environment. (b) Geometrical configuration of a pad-electrode embedded in layer (l) of a planar stratified medium.

where the plus sign applies when $z > z_p$, and the minus sign applies when $z < z_p$, $\bar{k}_s = \hat{x}k_x + \hat{y}k_y$ is the transverse wave vector, $\bar{r}_s = \hat{x}x + \hat{y}y$ is the transverse position vector, $\tilde{e}_l(\bar{k}_s)$ is the spectral amplitude of $E_{lz}(\bar{r})$. The wavenumber along the z direction, k_{lz}, satisfies the the dispersion relation $k_s^2 + k_{lz}^2 = k_l^2$ and the radiation condition $\mathrm{Im}(k_{lz}) > 0$. Here, $k_l^2 = \omega^2\mu_0\epsilon_0(\epsilon_l + i\sigma_l/\omega\epsilon_0)$, where ϵ_l and σ_l are the relative permittivity and conductivity of the lth layer, ϵ_0 and μ_0 are the permittivity and permeability of free space.

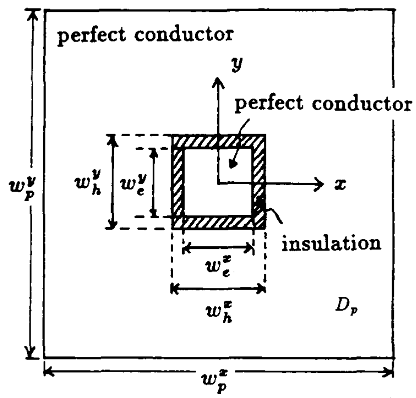

Fig. 2. Top view of the pad-electrode configuration.

In (1), $R_{\cup l}$ and $R_{\cap l}$ are the TM$_z$ reflection coefficients at the upper and lower boundaries of the lth layer, respectively. They can be obtained recursively as

$$R_{\cup l} = \frac{R_{l(l-1)} + R_{\cup(l-1)}e^{2ik_{(l-1)z}h_{l-1}}}{1 + R_{l(l-1)}R_{\cup(l-1)}e^{2ik_{(l-1)z}h_{l-1}}}$$

$$R_{\cap l} = \frac{R_{l(l+1)} + R_{\cap(l+1)}e^{2ik_{(l+1)z}h_{l+1}}}{1 + R_{l(l+1)}R_{\cap(l+1)}e^{2ik_{(l+1)z}h_{l+1}}} \tag{2}$$

where $R_{l(l\pm1)}$ is the Fresnel reflection coefficients from the lth layer to the $(l \pm 1)$th layer. The explicit form of $R_{l(l\pm1)}$ is

$$R_{l(l\pm1)} = \frac{(\epsilon_{l\pm1} + i\sigma_{l\pm1}/\omega\epsilon_0)k_{lz} - (\epsilon_l + i\sigma_l/\omega\epsilon_0)k_{(l\pm1)z}}{(\epsilon_{l\pm1} + i\sigma_{l\pm1}/\omega\epsilon_0)k_{lz} + (\epsilon_l + i\sigma_l/\omega\epsilon_0)k_{(l\pm1)z}}. \tag{3}$$

In the low-frequency limit, we have $\sigma_l \gg \omega\epsilon_l\epsilon_0$, then (3) reduces to

$$R_{l(l\pm1)} = \frac{\sigma_{l\pm1}k_{lz} - \sigma_l k_{(l\pm1)z}}{\sigma_{l\pm1}k_{lz} + \sigma_l k_{(l\pm1)z}}. \tag{3a}$$

In the electrostatic limit, the frequency is identically set to zero. We thus have $k_{lz} = k_{(l\pm1)z}$ for all l;, and (3a) reduces to

$$R_{l(l\pm1)} = \frac{\sigma_{l\pm1} - \sigma_l}{\sigma_{l\pm1} + \sigma_l}. \tag{3b}$$

The electrostatic potential $V_l(\bar{r})$ in the lth layer can be represented in the spectral domain as

$$\begin{aligned} V_l(\bar{r}) = \iint_{-\infty}^{\infty} d\bar{k}_s e^{i\bar{k}_s\cdot\bar{r}_s} \frac{i}{k_{lz}} \tilde{e}_l(\bar{k}_s) \\ \cdot \Bigg\{ e^{ik_{lz}|z-z_p|} - \frac{1}{1 - R_{\cup l}R_{\cap l}e^{2ik_{lz}h_l}} \\ \cdot [R_{\cup l}e^{ik_{lz}(-z-z_p-2d_{l-1})} - R_{\cup l}R_{\cap l}e^{ik_{lz}(-z+z_p+2h_l)} \\ + R_{\cap l}e^{ik_{lz}(z+z_p+2d_l)} - R_{\cup l}R_{\cap l}e^{ik_{lz}(z-z_p+2h_l)}] \Bigg\}. \end{aligned} \tag{4}$$

Using (1), the outflowing current density $J_z(\bar{r}_s)$ on the pad-electrode surface can be obtained as

$$J_z(\bar{r}_s) = \sigma_l[E_{lz}(\bar{r}_s, z=z_{p+}) - E_{lz}(\bar{r}_s, z=z_{p-})]$$
$$= \iint_{-\infty}^{\infty} d\bar{k}_s 2\sigma_l \tilde{e}_l(\bar{k}_s) e^{i\bar{k}_s \cdot \bar{r}_s}. \quad (5)$$

Expressing $J_z(\bar{r}_s)$ in terms of the two-dimensional Fourier transform, we have

$$J_z(\bar{r}_s) = \iint_{-\infty}^{\infty} d\bar{k}_s \tilde{J}_z(\bar{k}_s) e^{i\bar{k}_s \cdot \bar{r}_s}. \quad (6)$$

Thus the spectral amplitude $\tilde{J}_z(\bar{k}_s)$ is related to $\tilde{e}_l(\bar{k}_s)$ by $\tilde{e}_l(\bar{k}_s) = \tilde{k}_z(\bar{k}_s)/(2\sigma_l)$.

The electrostatic potential at any point $\bar{r}$ in layer (l) can then be represented in terms of $\tilde{J}_z(\bar{k}_s)$ as

$$V_l(\bar{r}) = \iint_{-\infty}^{\infty} d\bar{k}_s e^{i\bar{k}_s \cdot \bar{r}_s} g_{ll}(\bar{k}_s, z, z_p) \tilde{J}_z(\bar{k}_s) \quad (7)$$

where $g_{ll}(\bar{k}_s, z, z_p)$ is the scalar Green's function in the spectral domain. It can be represented in the following explicit form:

$$g_{ll}(\bar{k}_s, z, z') = \frac{i}{2\sigma_l k_{lz}} \left\{ e^{ik_{lz}|z-z'|} - \frac{1}{1 - R_{\cup l} R_{\cap l} e^{2ik_{lz}h_l}} \cdot [R_{\cup l} e^{ik_{lz}(-z-z'-2d_{l-1})} - R_{\cup l} R_{\cap l} e^{ik_{lz}(-z+z'+2h_l)} + R_{\cap l} e^{ik_{lz}(z+z'+2d_l)} - R_{\cup l} R_{\cap l} e^{ik_{lz}(z-z'+2h_l)}] \right\}. \quad (8)$$

With the Green's function formulation, the potential distribution satisfies the continuity conditions at the interfaces between layers. Imposing the remaining boundary condition on the pad-electrode surfaces where the potential is equal to the imposed voltage V_p, we obtain

$$\iint_{-\infty}^{\infty} d\bar{k}_s e^{i\bar{k}_s \cdot \bar{r}_s} g_{ll}(\bar{k}_s, z, z_p) \tilde{J}_z(\bar{k}_s) = V_p, \qquad \bar{r}_s \text{ on } D_p, \quad z = z_p \quad (9)$$

where D_p is the domain of the pad-electrode surface. Equation (9) is the integral equation to be used to solve for the outflowing current distribution.

By solving the integral equation (9), the outflowing current density distribution on the pad-electrode surface is obtained. Thus, the potential at any point in the layered medium can be calculated. The potential distribution in the mth layer due to the source in the lth layer can be represented in terms of the scalar Green's function $g_{ml}(\bar{k}_s, z, z')$ as follows:

$$V_m(\bar{r}) = \iint_{-\infty}^{\infty} d\bar{k}_s e^{i\bar{k}_s \cdot \bar{r}_s} g_{ml}(\bar{k}_s, z, z_p) \tilde{J}_z(\bar{k}_s). \quad (10)$$

When $m = 1$, $g_{ml}(\bar{k}_s, z, z_p)$ can be calculated by (8). When $m \neq l$, the scalar Green's function $g_{ml}(\bar{k}_s, z, z')$ can be calculated as follows:

Case(i) $z > z'$

$$g_{ml}(\bar{k}_s, z, z') = \frac{i}{2\sigma_l k_{lz}} X_{\cup m}[e^{ik_{mz}z_m} - R_{\cup m} e^{ik_{mz}(2h_m - z_m)}] \cdot \frac{e^{-ik_{lz}z_l'} - R_{\cap l} e^{ik_{lz}(2h_l + z_l')}}{1 - R_{\cup l} R_{\cap l} e^{2ik_{lz}h_l}} \quad (11)$$

where $z_m = z + d_m$, $z_l' = z' + d_{l-1}$. The upward transmission amplitude $X_{\cup m}$ can be calculated recursively by

$$X_{\cup m} = X_{\cup(m+1)} e^{ik_{(m+1)z}h_{m+1}} \frac{1 - R_{\cup(m+1)}}{1 - R_{\cup m} e^{2ik_{mz}h_m}} \quad (12)$$

where $m = l-2, l-3, \cdots, 0$. For $m = l-1$, we have

$$X_{\cup(l-1)} = \frac{1 - R_{\cup l}}{1 - R_{\cup(l-1)} e^{2ik_{(l-1)z}h_{l-1}}}. \quad (13)$$

Case(ii) $z < z'$

$$g_{ml}(\bar{k}_s, z, z') = \frac{i}{2\sigma_l k_{lz}} X_{\cap m}[e^{-ik_{mz}z_m} - R_{\cap m} e^{ik_{mz}(2h_m + z_m)}] \cdot \frac{e^{ik_{lz}z_l'} - R_{\cup l} e^{ik_{lz}(2h_l - z_l')}}{1 - R_{\cup l} R_{\cap l} e^{2ik_{lz}h_l}} \quad (14)$$

where $z_m = z + d_{m-1}$, $z_l' = z' + d_l$. The downward transmission amplitude $X_{\cap m}$ can be calculated recursively by

$$X_{\cap m} = X_{\cap(m-1)} e^{ik_{(m-1)z}h_{m-1}} \frac{1 - R_{\cap(m-1)}}{1 - R_{\cap m} e^{2ik_{mz}h_m}} \quad (15)$$

where $m = l+2, l+3, \cdots, t$. For $m = l+1$, we have

$$X_{\cap(l+1)} = \frac{1 - R_{\cap l}}{1 - R_{\cap(l+1)} e^{2ik_{(l+1)z}h_{l+1}}}. \quad (16)$$

III. Numerical Calculations

In this section, a method of moments is applied to solve (9) for the outflowing current distribution on the pad-electrode surface. It is difficult to find a set of global basis functions that is complete over the domain of the pad with a hole. Therefore, we use a set of local basis functions to represent the outflowing current distribution on the pad-electrode surface. The outflowing current distribution can thus be represented accurately by employing a reasonable number of these basis functions.

First, the domain of the pad-electrode is divided into small rectangular patches. The size of the patches can be adjusted to achieve the required accuracy.

The next step is to choose an appropriate set of local basis functions $R_j(\bar{r}_s)$, to represent the outflowing current distribution on the pad-electrode surface. $J_z(\bar{r}_s)$ can then be represented as a superposition of these basis functions $R_j(\bar{r}_s)$.

$$J_z(\bar{r}_s) = \sum_{j=1}^{N} \alpha_j R_j(\bar{r}_s - \bar{r}_{cj}) \quad (17)$$

where N is the total number of basis functions, α_j are the expansion coefficients to be determined, $\bar{r}_{cj}$ is the center coordinate of the jth basis function. Denote the Fourier transform of $R_j(\bar{r}_s)$ by $\tilde{R}_j(\bar{k}_s)$, hence the Fourier transform of $J_z(\bar{r}_s)$ can be represented as

$$\tilde{J}_z(\bar{k}_s)=\sum_{j=1}^{N} \alpha_j e^{-i\bar{k}_s\cdot \bar{r}_{cj}}\tilde{R}_j(\bar{k}_s). \tag{18}$$

Substituting (18) into (9), we get

$$\iint_{-\infty}^{\infty} d\bar{k}_s e^{i\bar{k}_s\cdot \bar{r}_s} g_{II}(\bar{k}_s, z, z_p) \sum_{j=1}^{N} \alpha_j e^{-i\bar{k}_s\cdot \bar{r}_{cj}}\tilde{R}_j(\bar{k}_s)=V_p, \quad \bar{r}_s \text{ on } D_p, \quad z=z_p. \tag{19}$$

We employ a Galerkin's approach by using the same set of basis functions as the testing functions. Taking the inner product of the ith testing function with (19), we obtain

$$\sum_{j=1}^{N} Z_{ij}\alpha_j=\beta_i \tag{20}$$

where

$$Z_{ij}=\iint_{-\infty}^{\infty} d\bar{k}_s e^{i\bar{k}_s\cdot(\bar{r}_{ci}-\bar{r}_{cj})} g_{II}(\bar{k}_s, z_p, z_p)\tilde{R}_i(-\bar{k}_s)\tilde{R}_j(\bar{k}_s) \tag{21}$$

$$\beta_i=\frac{V_p}{(2\pi)^2}\iint_{-\infty}^{\infty} d\bar{r}_s R_i(\bar{r}_s-\bar{r}_{ci}). \tag{22}$$

The expansion coefficients α_j can be solved by inverting (20).

Choosing the unit pulse function as the basis function, we have

$$R_i(\bar{r}_s)=\begin{cases}1, & -a_i/2\le x\le a_i/2, \ -b_i/2\le y\le b_i/2\\ 0, & \text{elsewhere}\end{cases} \tag{23}$$

where a_i and b_i are the width of the ith patch along the x and y direction, respectively. The Fourier transform of $R_i(\bar{r}_s)$ is thus given by

$$\tilde{R}_i(\bar{k}_s)=\frac{\sin(k_x a_i/2)\sin(k_y b_i/2)}{\pi^2 k_x k_y}. \tag{24}$$

Observing that $\tilde{R}_i(\bar{k}_s)$ is an even function of both k_x and k_y, the double integral in (21) over the whole $k_z - k_y$ plane can be reduced to an integral over the first quadrant as

$$Z_{ij}=4\int_0^{\infty} dk_x \int_0^{\infty} dk_y \cos k_x(x_{ci}-x_{cj})\cos k_y(y_{ci}-y_{cj}) \cdot g_{II}(\bar{k}_s, z_p, z_p)\tilde{R}_i(\bar{k}_s)\tilde{R}_j(\bar{k}_s) \tag{25}$$

where $\bar{r}_{ci} = \hat{x}x_{ci} + \hat{y}y_{ci}$, $\bar{r}_{cj} = \hat{x}x_{cj} + \hat{y}y_{cj}$.

From (25), it is clear that $Z_{ij} = Z_{ji}$. This property is utilized to reduce the computation time by about one half. In the electrostatic limit, the Green's function in (8) possesses a singularity at $k_p = |\bar{k}_s| = 0$, which is integrable. To perform the integration in (25), we divide the first quadrant in the $k_x - k_y$ plane into two parts. The first part is $0 \le k_x \le \Delta_x$, $0 \le k_y \le \Delta_y$, and the second part is the remaining portion of the first quadrant. The integration over the first part is given by

$$\begin{aligned}&\int_0^{\Delta x} dk_x \int_0^{\Delta y} dk_y \cos k_x(x_{ci}-x_{cj}) \cdot \cos k_y(y_{ci}-y_{cj}) g_{II}(\bar{k}_s, z_p, z_p)\tilde{R}_i(\bar{k}_s)\tilde{R}_j(\bar{k}_s)\\ &=\int_0^{\Delta x} dk_x \int_0^{\Delta y} dk_y \left\{\cos k_x(x_{ci}-x_{cj}) \cdot \cos k_y(y_{ci}-y_{cj}) g_{II}(\bar{k}_s, z_p, z_p)\tilde{R}_i(\bar{k}_s)\tilde{R}_j(\bar{k}_s)-\frac{\gamma_{ij}}{k_\rho}\right\}\\ &\quad+\gamma_{ij}\int_0^{\Delta x} dk_x \int_0^{\Delta y} dk_y \frac{1}{k_\rho}\end{aligned} \tag{26}$$

where γ_{ij} is the residue calculated by

$$\gamma_{ij}=\lim_{k_\rho\to 0} k_\rho \cos k_x(x_{ci}-x_{cj}) \cdot \cos k_y(y_{ci}-y_{cj}) g_{II}(\bar{k}_s, z_p, z_p)\tilde{R}_i(\bar{k}_s)\tilde{R}_j(\bar{k}_s). \tag{27}$$

The second integral on the right side of (26) can be performed analytically, to obtain

$$\int_0^{\Delta x} dk_x \int_0^{\Delta y} dk_y \frac{1}{k_\rho}=\Delta_x \ln\left[\frac{\Delta_y}{\Delta_x}+\sqrt{1+\left(\frac{\Delta_y}{\Delta_x}\right)^2}\right] +\Delta_y \ln\left[\frac{\Delta_x}{\Delta_y}+\sqrt{1+\left(\frac{\Delta_x}{\Delta_y}\right)^2}\right]. \tag{28}$$

The choice of Δ_x and Δ_y is arbitrary, and does not affect the final value of the integral in (25). In the numerical computation of the second part of the above integral, we gradually increased the domain of integration until convergence was achieved.

To perform the numerical integration more efficiently, we store the computations which are repeatedly used, hence reducing the CPU time significantly. All the numerical results presented in the next section were calculated using a VAX/750.

We choose to compute the above double integral in the cartesian coordinate system rather than the polar system, because of the fact that as k_ρ increases, one requires a finer mesh along the ϕ direction. This multigridding required in the polar coordinate system, makes the bookkeeping process very cumbersome.

To find the current density distribution at any point in an arbitrary layer (m), we have

$$\bar{J}_m(\bar{r})=-\sigma_m\nabla V_m(\bar{r}), \qquad m=0, 1, 2, \cdots, t. \tag{29}$$

To calculate the current density in (29), we first substitute (18) and (24) into (10), then apply (29). Utilizing the following symmetrical properties of the basis functions,

$$\tilde{R}(-k_x, k_y)=\tilde{R}(k_x, k_y), \quad \tilde{R}(k_x, -k_y)=\tilde{R}(k_x, k_y) \tag{30}$$

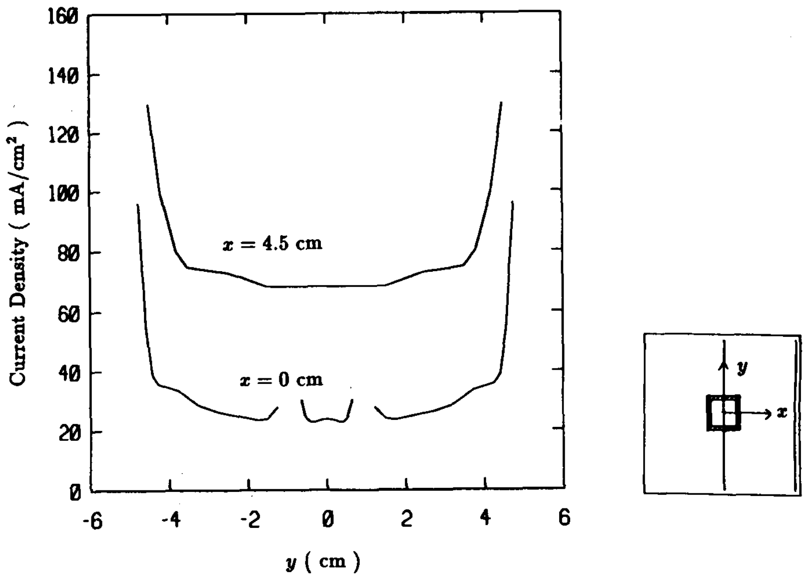

Fig. 3. Outflowing current distribution on a pad-electrode surface in a homogeneous medium with σ = 10 S/m, $w_p^x = w_p^y$ = 10 cm, $w_h^x = w_h^y$ = 2 cm, $w_e^x = w_e^y$ = 1.6 cm, $V_p = V_e$ = 1V.

we have

$$J_{mx}(\bar{r}) = 4\sigma_m \sum_{j=1}^{N} \alpha_j \int_0^\infty dk_x k_x \sin k_x(x - x_{cj}) \frac{\sin k_x a_j/2}{\pi k_x} \cdot \int_0^\infty dk_y \cos k_y(y - y_{cj}) \frac{\sin k_y b_j/2}{\pi k_y} g_{ml}(\bar{k}_s, z, z_p) \quad (31)$$

$$J_{my}(\bar{r}) = 4\sigma_m \sum_{j=1}^{N} \alpha_j \int_0^\infty dk_x \cos k_x(x - x_{cj}) \frac{\sin k_x a_j/2}{\pi k_x} \cdot \int_0^\infty dk_y k_y \sin k_y(y - y_{cj}) \frac{\sin k_y b_j/2}{\pi k_y} g_{ml}(\bar{k}_s, z, z_p) \quad (32)$$

$$J_{mz}(\bar{r}) = -4\sigma_m \sum_{j=1}^{N} \alpha_j \int_0^\infty dk_x \cos k_x(x - x_{cj}) \frac{\sin k_x a_j/2}{\pi k_x} \cdot \int_0^\infty dk_y \cos k_y(y - y_{cj}) \frac{\sin k_y b_j/2}{\pi k_y} \frac{\partial g_{ml}(\bar{k}_s, z, z_p)}{\partial z} \quad (33)$$

where $m = 0, 1, 2, \cdots, t$.

IV. Results and Discussion

In the numerical results presented in this section, we choose the pad-electrode dimensions such that $w_p^x = w_p^y = 10$ cm, $w_h^x = w_h^y = 2$ cm, $w_e^x = w_e^y = 1.6$ cm. The electrode is patched by 25 unit pulse functions with equal patch size of 0.32 by 0.32 cm each. The pad surface is patched by 96 unit pulse functions with equal patch size of 1 by 1 cm.

The pad-electrode structure is first assumed to be buried in a homogeneous medium with $\sigma = 10$ S/m. The magnitude of the outflowing current distribution on the pad-electrode surface along $x = 0$ cm and $x = 4.5$ cm are displayed in Fig. 3. The edge effect is obvious near the edge of the pad and the electrode, but is not so pronounced near the edge of the hole.

Next, consider the case of a three-layer medium with both layer (0) and layer (2) as semi-infinite half-space, and the thickness of layer (1) is $h = 10$ cm. The conductivity of layer (1) is $\sigma_1 = 10$ S/m, and the conductivities of layers (0) and (2) are the same as σ_0. The pad-electrode structure is buried in the middle of layer (1) as shown in Fig. 4. The normalized total electrode current on a log scale, log (I_e/I_{e0}), is plotted as a function of log (σ_0/σ_1), where I_{e0} is a reference value taken to be the total electrode current for the case of a homogeneous medium with $\sigma_0 = 10$ S/m.

Two cases are displayed with layer thickness $h = 10$ cm and $h = 2$ cm. It is observed that the total electrode current increases with σ_0. The total electrode current with $h = 2$ cm is more sensitive to the change of σ_0 than that with $h = 10$ cm. When $\sigma_0/\sigma_1 < 1$, the total electrode current is larger for $h = 10$ cm than for $h = 2$ cm, since for the case with $h = 10$ cm, a larger effective volume of higher conductivity medium is included than the other case. Similarly, it is observed that when $\sigma_0/\sigma_1 > 1$, the total electrode current is smaller for $h = 10$ cm than it is for $h = 2$ cm.

In this kind of measurement environment, the total electrode current is sensitive to both h and σ_0. The total electrode current can be used to predict the conductivity σ_0 if the standoff thickness h can be estimated.

In Fig. 5, the total electrode current I_e is displayed as a function of the layer thickness h. The conductivity of layer (1) is $\sigma_1 = 10$ S/m, and the conductivity of layers (0) and (2) are the same with a value equals σ_0. Two cases with $\sigma_0 = 1$ S/m and $\sigma_0 = 10^{-3}$ S/m are displayed. It is observed that the total electrode current I_e increases with layer thickness h. The magnitude of I_e with $\sigma_0 = 1$ S/m is about 10 times larger than that with $\sigma_0 = 10^{-3}$ S/m.

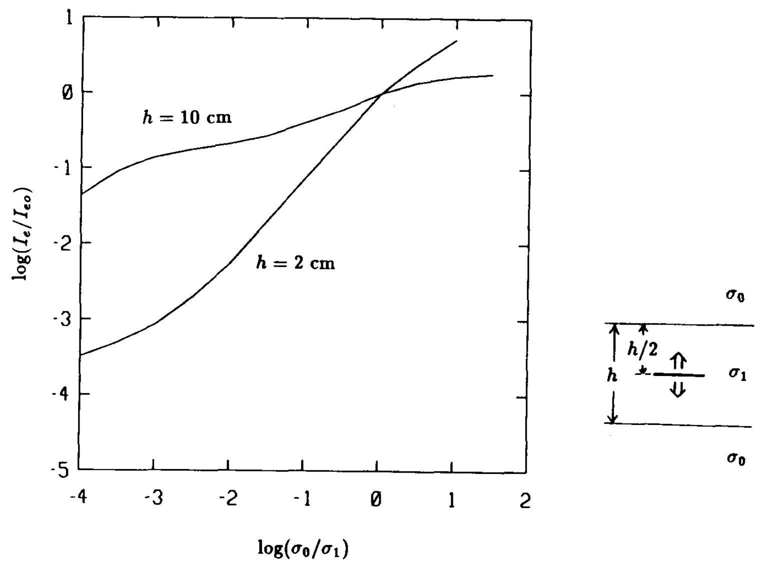

Fig. 4. Total electrode current of a pad-electrode in a three-layer medium, $w_p^x = w_p^y = 10$ cm, $w_h^x = w_h^y = 2$ cm, $w_e^x = w_e^y = 1.6$ cm, $V_p = V_e = 1$ V, $\sigma_1 = 10$ S/m, I_{eo} is the total electrode current in a homogeneous medium with $\sigma = 10$ S/m.

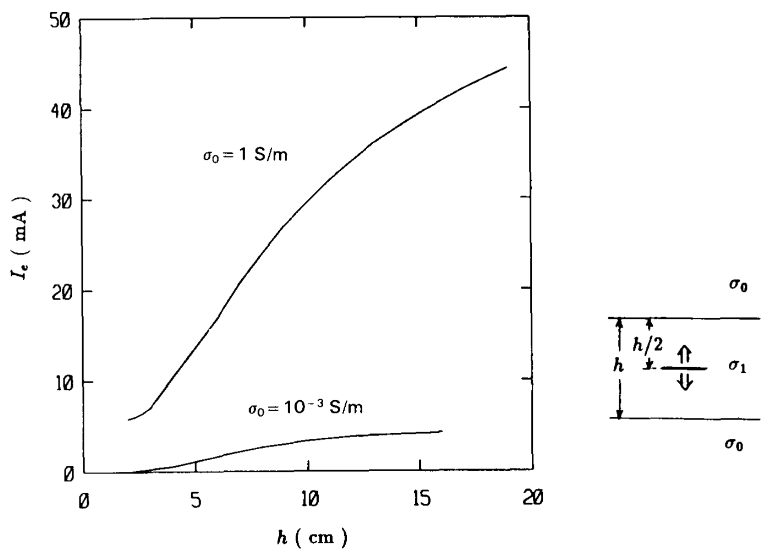

Fig. 5. Total electrode current of a pad-electrode in a three-layer medium, $w_p^x = w_p^y = 10$ cm, $w_h^x = w_h^y = 2$ cm, $w_e^x = w_e^y = 1.6$ cm, $V_p = V_e = 1$ V, $\sigma_1 = 10$ S/m.

In Fig. 6, the current density $J_z(\rho = 0, h^+/2)$ at the interface between layer (0) and layer (1) is evaluated as a function of log (σ_0/σ_1) with $\sigma_1 = 10$ S/m. The current density is normalized to the current density in a homogeneous medium at a point 1 cm right above the electrode center. When $\sigma_0/\sigma_1 > 1$, the current density is larger for $h = 2$ cm than for $h = 10$ cm.

In Fig. 7, the electric field strength $E_z(\rho = 0, h^+/2)$ at the interface between layer (0) and layer (1) is displayed as a function of layer thickness h. The conductivity of layer (1) is 10 S/m, the conductivities of layers (0) and (2) are the same as σ_0. Two cases with $\sigma_0 = 1$ S/m and $\sigma_0 = 10^{-3}$ S/m are calculated. The field strength decreases as the layer thickness h increases. The field strength is about four times larger for $\sigma_0 = 1$ S/m than for $\sigma_0 = 10^{-3}$ S/m.

In Fig. 8, layer (0) is a conductive half-space of a high conductivity $\sigma_0 = 10^6$ S/m, layer (1) is a resistive layer with $\sigma_1 = 10^{-3}$ S/m and $h_1 = 2$cm. The insulator in layer (1) and the

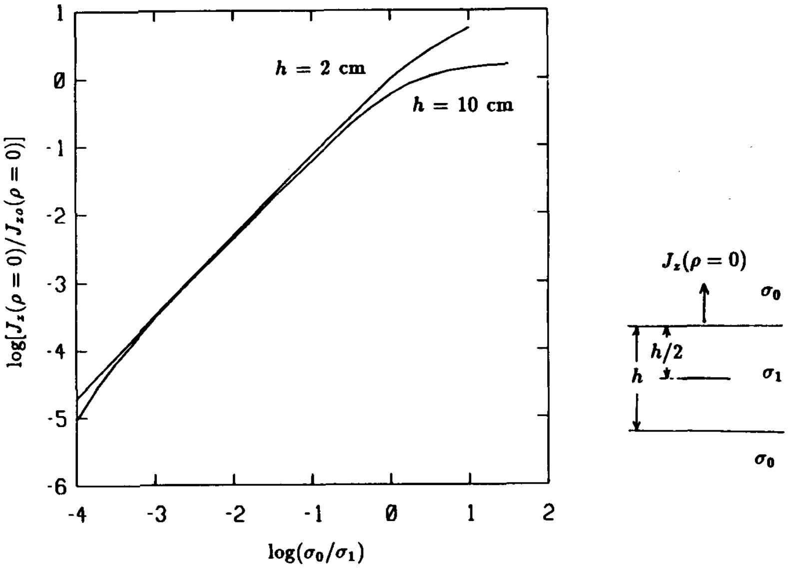

Fig. 6. Current density at the interface of a three-layer medium, $w_p^x = w_p^y = 10$ cm, $w_h^x = w_h^y = 2$ cm, $w_e^x = w_e^y = 1.6$ cm, $V_p = V_e = 1$ V, $\sigma_1 = 10$ S/m, $J_{zo}(\rho = 0)$ is the current density at 2 cm above the electrode with $\sigma_0 = 10$ S/m.

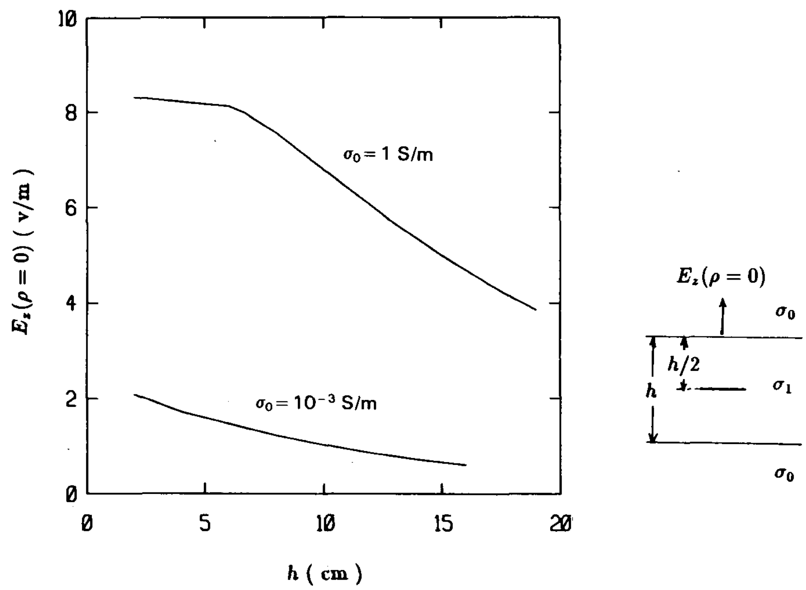

Fig. 7. Electric field at the interface of a three-layer medium, $w_p^x = w_p^y = 10$ cm, $w_h^x = w_h^y = 2$ cm, $w_e^x = w_e^y = 1.6$ cm, $V_p = V_e = 1$ V, $\sigma_1 = 10$ S/m.

good conductor in layer (0) have the effect of focusing the current flow into the rock formation. Layer (2) is a standoff layer with $\sigma_2 = 10$ S/m and variable thickness h_2. The pad-electrode is located at the interface between layer (1) and layer (2). The region below layer (2) possesses different possible conductivity profiles, and can be modeled by a multilayered medium. The origin of the coordinate system is chosen at the interface between the standoff layer and the conductivity profile, right below the electrode center. The conductivity profiles used in this paper include step profile, linear profile, parabolic profile, and inversion profile. For a step profile,

$$\sigma_s(z) = \sigma_b, \qquad z \leq 0 \tag{34}$$

where σ_b is a constant conductivity.

For a linear profile,

$$\sigma_l(z) = \begin{cases} \sigma_b + (\sigma_2 - \sigma_b)(1 + z/D), & -D \leq z \leq 0 \\ \sigma_b, & z < -D \end{cases} \tag{35}$$

where D is the depth of the conductivity profile, σ_b is the

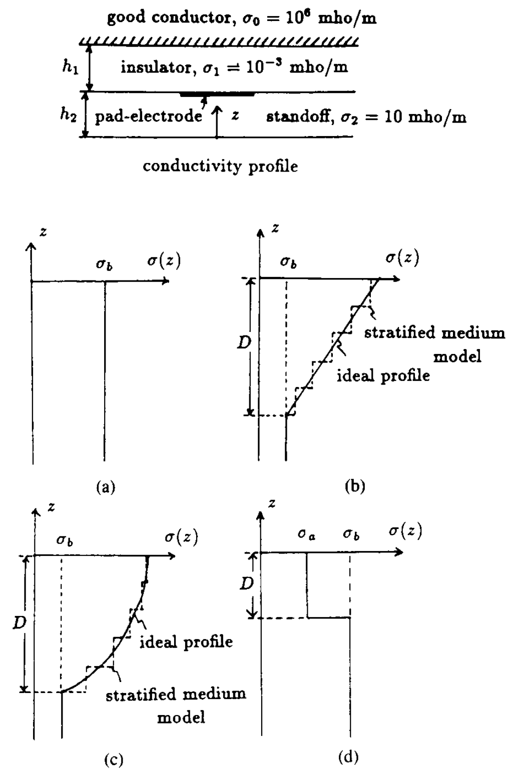

Fig. 8. Configuration of a pad-electrode in a profiled layered medium, $w_p^x = w_p^y = 10$ cm, $w_h^x = w_h^y = 2$ cm, $w_e^x = w_e^y = 1.6$ cm, $V_p = V_e = 1$ V. (a) Step profile. (b) Linear profile. (c) Parabolic profile. (d) Inversion profile.

background conductivity in the region $z < -D$ which is homogeneous by assumption.

For a parabolic profile,

$$\sigma_p(z) = \begin{cases} \sigma_b + (\sigma_2 - \sigma_b)[1 - z/D)^2], & -D \le z \le 0 \\ \sigma_b, & z < -D \end{cases} \tag{36}$$

where the definition of D and σ_b is the same as that for the linear profile.

For an inversion profile,

$$\sigma_i(z) = \begin{cases} \sigma_a, & -D \le z \le 0 \\ \sigma_b, & z < -D \end{cases} \tag{37}$$

where σ_a is the conductivity of the inversion layer and σ_b is the conductivity of the background medium. Note that $\sigma_a < \sigma_b$.

For both the linear profile and the parabolic profile, a multilayered medium is used to model the conductivity profile. The region $-D \le z \le 0$ is first divided into a multilayered medium with the same thickness for each layer. The conductivity of each layer assumes the value calculated from either (35) or (36) at the middle of that layer.

The total electrode current of the pad-electrode in a step conductivity profile is displayed in Fig. 9 as a function of the standoff thickness h_2. The total electrode current is plotted on a log scale normalized to I_{eo} which is a reference electrode current with $\sigma_b = 10$ S/m in Fig. 8(a). The thickness of the standoff layer ranges from 0 to 2 cm, and σ_b ranges from 0.1 to 100 S/m. It is observed that the total electrode current is almost a linear function of σ_b at any standoff thickness. Furthermore, the total electrode current is insensitive to the variation of h_2.

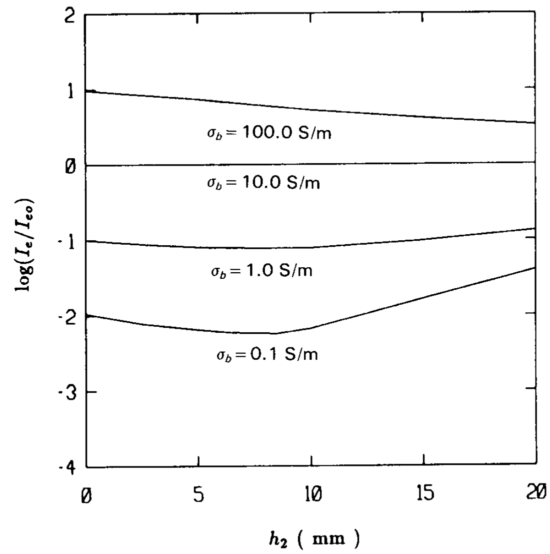

Fig. 9. Total electrode current of a pad-electrode with a step conductivity profile, $w_p^x = w_p^y = 10$ cm, $w_h^x = w_h^y = 2$ cm, $w_e^x = w_e^y = 1.6$ cm, $V_p = V_e = 1$ V, $h_1 = 2$ cm, I_{eo} is the total electrode current when $\sigma_b = 10$ S/ m.

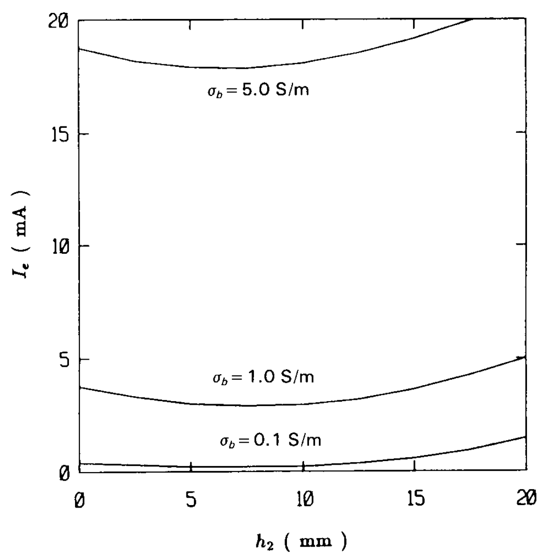

Fig. 10. Total electrode current of a pad-electrode with a step conductivity profile, $w_p^x = w_p^y = 10$ cm, $w_h^x = w_h^y = 2$ cm, $w_e^x = w_e^y = 1.6$ cm, $V_p = V_e = 1$ V, $h_1 = 2$ cm.

The total electrode current for the step conductivity profile is also plotted on a normal scale in Fig. 10 to compare with the other conductivity profiles. Three cases of background conductivities are used: $\sigma_b = 0.1$ S/m, $\sigma_b = 1.0$ S/m, and $\sigma_b = 5.0$ S/m. The total electrode current exhibits a minimum as a function of h_2.

Next, the total electrode current of the pad-electrode in the

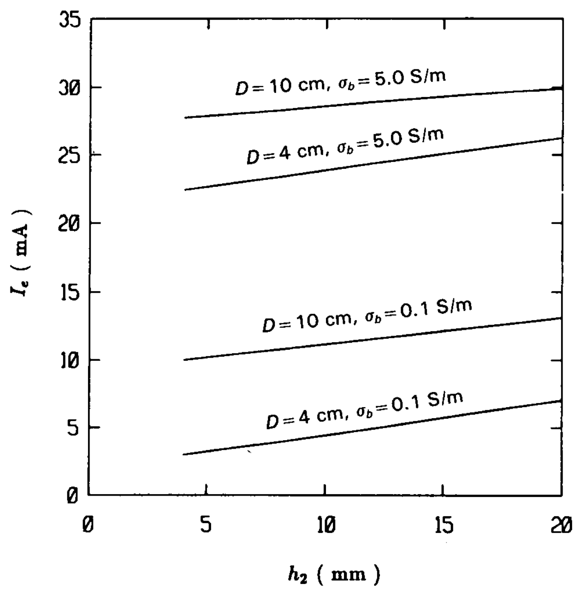

Fig. 11. Total electrode current of a pad-electrode with a linear conductivity profile, $w_p^x = w_p^y = 10$ cm, $w_h^x = w_h^y = 2$ cm, $w_e^x = w_e^y = 1.6$ cm, $V_p = V_e = 1$ V, $h_1 = 2$ cm.

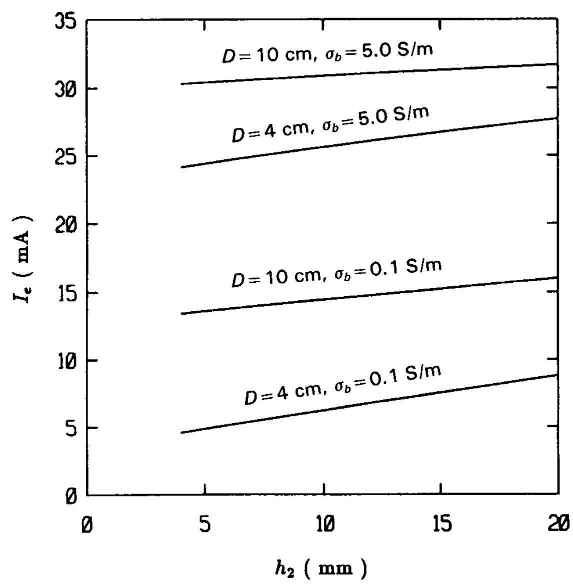

Fig. 12. Total electrode current of a pad-electrode with a parabolic conductivity profile, $w_p^x = w_p^y = 10$ cm, $w_h^x = w_h^y = 2$ cm, $w_e^x = w_e^y = 1.6$ cm, $V_p = V_e = 1$ V, $h_1 = 2$ cm.

case of a linear conductivity profile is displayed in Fig. 11 as a function of the standoff thickness h_2. The thickness of the standoff layer ranges from 0 to 2 cm. Two σ_b of 0.1 S/m and 5 S/m, and two profile depths of $D = 4$ and 10 cm are chosen.

From Fig. 11, it is observed that the electrode current is insensitive to the variation of h_2. The electrode current is mainly affected by the background conductivity σ_b and profile depth D. Increasing either D or σ_b will increase the total electrode current.

Similarly, the total electrode current of the pad-electrode in a parabolic conductivity profile is displayed in Fig. 12 as a function of the standoff thickness h_2. The current is plotted on a normal scale. The thickness of the standoff layer ranges from 0 to 2 cm. Two σ_b of 0.1 S/m and 5 S/m, and two profile depths of $D = 4$ and 10 cm are chosen.

Similar to the result for the linear profile, the total electrode current for a parabolic profile is insensitive to the variation of h_2. The total electrode current is mainly affected by the background conductivity σ_b and the profile depth D. Increasing either D or σ_b will increase the total electrode current.

The total electrode current is larger in Fig. 12 compared with that in Fig. 11 having the same background conductivity and profile depth. For both linear profile and parabolic profile, the total electrode current increases as h_2 increases.

For both the linear and parabolic profiles, the background conductivity σ_b can be retrieved from the total electrode current if the profile is linear or parabolic, and if the depth can be estimated independently.

Finally, consider the inversion profile with $D = 1$ cm or $D = 3$ cm. Five combinations of (σ_a, σ_b) are used, these are $(\sigma_a, \sigma_b) = (0.05, 0.1)$, (0.1, 1.0), (0.5, 1.0), (1.0, 5.0), and (2.5, 5.0), all in S/m. The total electrode current versus the standoff thickness h_2 is plotted in Fig. 13(a) for $D = 1$ cm, and in Fig. 13(b) for $D = 3$ cm.

It is observed that increasing either σ_a or σ_b will increase the electrode current, and increasing the profile depth D will decrease the electrode current especially when σ_a or σ_b is large. The total electrode current increases when h_2 is either increased or decreased. This is similar to the results for the step profile.

Comparing Fig. 10 with Figs. 11 and 12, it is observed that when σ_b is increased, the increasing rate of the total electrode current for the step profile is larger than that for the linear profile or the parabolic profile. The increasing rate is larger when the profile depth is smaller. This can be explained as follows. Since the linear profile and the parabolic profile have a transition region between the standoff layer and the background medium, the effect of σ_b to the total electrode current is shielded by the transition region. On the contrary, the background medium in the step profile is right below the standoff layer, hence it affects the total electrode current more directly.

V. Conclusion

An electro-quasistatic approach in the spectral domain is derived to analyze a pad-electrode antenna used in the applications of low frequency geophysical probing. An integral equation is derived, which is then solved by the method of moments. A set of unit pulse functions are used to represent the outflowing current distribution on the pad-electrode surface. The potential distribution in the layered medium can be calculated in terms of the outflowing current distribution.

Numerical results for a symmetrical three-layer medium is presented. The effects of layer thickness and conductivity is studied. A more practical measurement environment with four different kinds of conductivity profiles are then investigated. The effects of standoff thickness, background conductivity, and profile depth are studied. Numerical results reveal that the total electrode current is sensitive to the conductivity of the

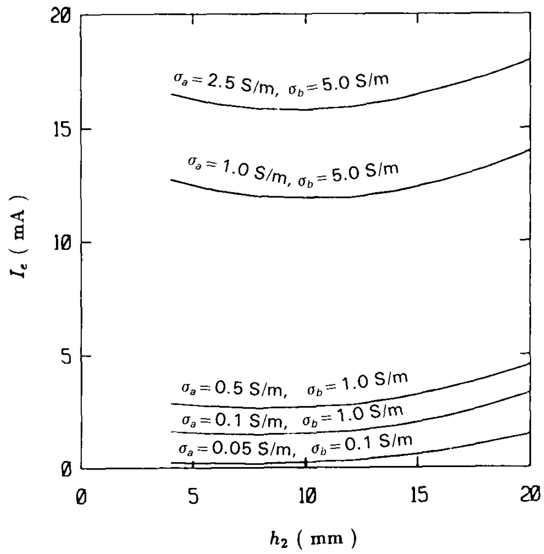

(a)

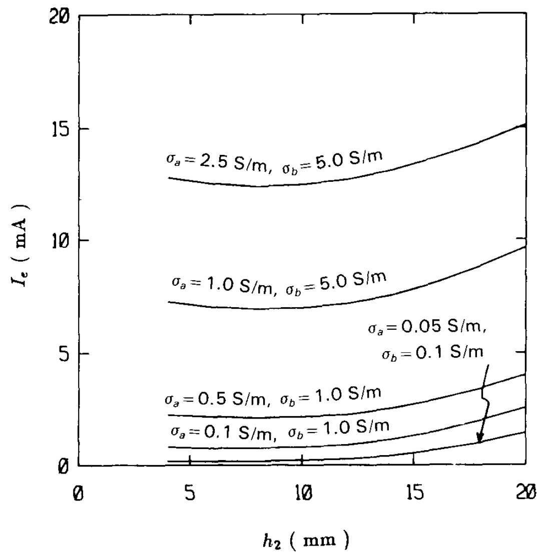

(b)

Fig. 13. (a)Total electrode current of a pad-electrode with an inversion conductivity profile (D = 1 cm), $w_p^x = w_p^y = 10$ cm, $w_h^x = w_h^y = 2$ cm, $w_e^x = w_e^y = 1.6$ cm, $V_p = V_e = 1$ V, $h_1 = 2$ cm. (b) Total electrode current of a pad-electrode with an inversion conductivity profile (D = 3 cm), $w_p^x = w_p^y = 10$ cm, $w_h^x = w_h^y = 2$ cm, $w_e^x = w_e^y = 1.6$ cm, $V_p = V_e = 1$ V, $h_1 = 2$ cm.

formation medium, but is insensitive to the standoff thickness. Thus, it can be used to retrieve the background conductivity for different types of conductivity profiles, which is very useful in geophysical probing.

Acknowledgment

The authors wish to thank Dr. S. M. Ali for many valuable discussions.

References

[1] L. M. Al'pin, M. N. Berdichevskii, G. A. Vedrintsev, and A. M. Zagarmistr, "Dipole Methods for Measuring Earth Conductivity," Consultants Bureau, New York, 1966.

[2] O. Koefoed, *Geosounding Principles, 1—Resistivity Sounding Measurements.* New York: Elsevier, 1979.

[3] G. Kunetz, *Principles of Direct Current Resistivity Prospecting.* Berlin, West Germany: Gebruder Borntraeger, 1966.

[4] L. L. Nettleton, *Geophysical Prospecting for Oil.* New York: McGraw-Hill, 1940.

[5] J. R. Wait, *Geo-Electromagnetism.* New York: Academic, 1982.

[6] L. Tsang and J. A. Kong, "Electromagnetic fields due to a horizontal electric dipole antenna laid on the surface of a two-layer medium," *IEEE Trans. Antennas Propagat.*, vol. AP-22, no. 5, pp. 709-711, Sept. 1974.

[7] D. Cheng, J. A. Kong, and L. Tsang, "Geophysical subsurface probing of a two-layered uniaxial medium with a horizontal magnetic dipole," *IEEE Trans. Antennas Propagat.*, vol. AP-25, no. 6, pp. 766-769, Nov. 1977.

[8] B. Banerjee, B. J. Sengupta, and B. P. Pal, "Apparent resistivity of a multi-layered earth with a layer having exponentially varying conductivity," *Geophys. Prospect.*, vol. 28, pp. 435-452, 1980.

[9] J. A. Kong, *Research Topics in Electromagnetic Wave Theory.* New York: Wiley, 1981, ch. 10.

[10] —, *Electromagnetic Wave Theory.* New York: Wiley, 1986.

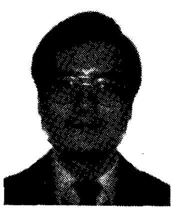

Jean-Fu Kiang was born in Taipei, Taiwan, Republic of China, on February 2, 1957. He received the B.S. and M.S. degrees in electrical engineering from National Taiwan University in 1979 and 1981, respectively, and the Ph.D. degree in electrical engineering from the Massachusetts Institute of Technology in 1988.

From 1983, he was a Research and Teaching Assistant in the Department of Electrical Engineering and Computer Science at the Massachusetts Institute of Technology, Cambridge. His research interests are electromagnetic theory, applications, and numerical analysis.

Mr. Kiang is a member of Sigma Xi.

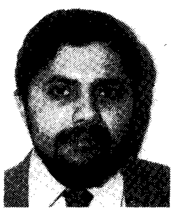

Tarek M. Habashy (S'79–M'83) was born in Cairo, Egypt. He received the B.Sc. degree from Cairo University, Egypt, and the M.Sc. and Ph.D. degrees from the Massachusetts Institute of Technology, Cambridge, in 1976, 1980 and 1983, respectively, all in electrical engineering. During the academic year 1982-1983, he was a Postdoctoral Research Associate in the Department of Electrical Engineering and Computer Science at MIT.

Since September 1983, he has been with Schlumberger-Doll Research, as a member of the professional staff and is now the program leader of the Applied Electromagnetics Program, conducting research on inverse scattering and electromagnetic well-logging techniques.

Dr. Habashy is currently serving as a member of the Editorial Board of the *Journal of Electromagnetic Waves and Applications* (JEWA). He is a member of AGU and Commission B of URSI.

Jin Au Kong (S'65–M'69–SM'74–F'85) is Professor of Electrical Engineering and Chairman of Area IV on Energy and Electromagnetic Systems in the Department of Electrical Engineering and Computer Science at the Massachusetts Institute of Technology in Cambridge, MA. In 1977–1980 he served the United Nations as a High-Level Consultant to the Under Secretary-General on science and technology, and as an Interregional Advisor on remote sensing technology for the Department of Technical Cooperation for Development. His research interest is in the area of electromagnetic wave theory and applications. He has published five books, 123 refereed journal articles, and 125 conference papers, and supervised 77 theses. He is currently a member of the Advisory Council for the Electrical Engineering Department at the University of Pennsylvania, a consultant to the MIT Lincoln Laboratory, the Editor for the Wiley series in remote sensing, the Editor-in-Chief of the *Journal of Electromagnetic Waves and Applications* (JEWA), and the Chief Editor for the Elsevier book series on Progress in Electromagnetics Research (PIER).